Chemical Durability of Multicomponent Lanthanide Zirconate Solid Solutions

Keith Bryce[1], Kun Yang[1], Tiankai Yao[3], Jie Lian[1,2]*

1. Department of Mechanical, Aerospace and Nuclear Engineering, Rensselaer Polytechnic Institute, NY 12180, USA

2. Department of Materials Science & Engineering, Rensselaer Polytechnic Institute, NY 12180, USA

3. Idaho National Laboratory

* Corresponding author, Email: lianj@rpi.edu

Abstract

Multicomponent zirconate solid solutions $A_2Zr_2O_7$ (A= (Sm,Yb), (Sm,Yb,Gd), (Sm,Yb,Gd,Er), and (Sm,Yb,Gd,Er,Dy)) were synthesized through spark plasma sintering and their chemical durability was investigated *via* semi-dynamic leaching tests in pH = 1 nitric acid at 90 °C. Incongruent dissolution occurred for all samples with preferential elemental releases of zirconium in all $A_2Zr_2O_7$ except for high entropy (Sm,Yb,Gd,Er,Dy)Zr_2O_7 which displays a congruent release of the A-site elements and Zr. Post-leaching TEM analysis of the high entropy zirconate revealed a 5~8 nm thick passivation film consisting of partial amorphous and nano-sized fluorite domains. A strong positive correlation was found between the lanthanide elemental release rates and the A-site cation size disorder, whereas a negative correlation was observed between the elemental release rates and mixing entropy. These results demonstrate that the cationic size disorder and mixing entropy significantly impact on the chemical durability of the multicomponent oxide solid solutions, and with more controlled design parameters, improvements in the corrosion resistance of these materials may be achieved.

1. Introduction

The disposal of nuclear waste is a complex issue that requires the use of metal, glass, and ceramic materials for the immobilization of long-lived radionuclides. The use of deep geological repositories has been widely adopted for the isolation and disposal of high-level nuclear waste.

Once spent fuel is processed and separated into appropriate waste streams, they may be combined with various additives to produce waste glasses and ceramics which are then sealed in stainless steel canisters and placed in the repository [1, 2]. One of the more widely studied waste ceramics is SYNROC, a multiphase combination of minerals such as zirconolite, pyrochlore, perovskite, and hollandite, created by mixing radioactive waste calcine (a fine-grained mixture of radioactive oxides) with inert oxides and hot-pressing the mixture in a sealed metal container to create a dense and compact material [1]. The pyrochlore phase is generally accepted as the base waste form phase for immobilizing multivalent uranium, plutonium, and transuranic actinides due to its structural flexibility and the ability of its natural analogous minerals to retain various high-level waste elements over large time scales [3].

Pyrochlores (space group *F*-$d\bar{3}m$) are indicated by the structural formula $A_2B_2O_7$ (A^{3+} = rare-earth ions La to Lu; B^{4+} = Ti, Zr, Sn, Hf, etc.) and are a derivative of the fluorite structure AO_2 (e.g., cubic ZrO_2) except that two metal cations are being ordered at the cation sublattices and an oxygen vacancy at O(8a) while the seven oxygen atoms are located at two different sites (O_{48f} and O'8b) [4]. Another derivative of the fluorite structure and close relative to the pyrochlore structure is the defect fluorite structure $A_2Zr_2O_7$ (*Fm*-$\bar{3}m$). It is isostructural as the cubic ZrO_2 lattice but with the lanthanide and Zr ions randomly distributed on the Zr-sites and 7/8th of the 8c oxygen sublattice occupied as shown in Fig. 1(b) [5, 6]. The seven oxygen atoms on the anion sublattice are tetrahedrally coordinated by four random cations and evenly distributed over eight equivalent sites [7]. Through control of the ionic radius of the cations at the A- and B-sites, the phase stability and structure of the $A_2B_2O_7$ (*Fd*-$\bar{3}m$) compositions can be well controlled. Depending on the ionic radius ratio of A/Zr, $A_2Zr_2O_7$ may be stabilized as the pyrochlore structure if r_A/r_{Zr} is in the range of 1.48−1.78 while the defect fluorite is stabilized if r_A/r_{Zr} is less than 1.48 [8, 9, 10]. However, other environmental factors including temperature, pressure, and radiation dose may also affect the structural stability of these phases [11, 12, 13].

The ability of these matrixes to retain radionuclides over a large time scale under geological repository conditions is directly correlated to their phase stability and chemical durability. Lab-scale leaching tests are generally employed to evaluate the chemical durability and corrosion resistance of waste form materials. Yang et. al. (2021) investigated the chemical durability of a series of zirconate fluorites and pyrochlores $A_2Zr_2O_7$ (A = La, Nd, and Sm to

Yb) *via* semi-dynamic leaching tests in pH = 1 nitric acid at 90 °C [14]. The results showed a gradual reduction in the dissolution rates as the A-site cations changed from La to Yb and an incongruent dissolution behavior where the A/Zr ratios in the leachate by solution chemistry analysis were significantly lower than the stoichiometric ratio, particularly for the more corrosion-resistant materials such as $Er_2Zr_2O_7$ and $Yb_2Zr_2O_7$. In the case of $Er_2Zr_2O_7$, this led to the preferential release of Zr and the formation of an Er-enriched surface passivation film, which is not consistent with the expectation of the preferential release of the lanthanides due to their weaker metal oxide bond. This suggests that further knowledge of the corrosion kinetics of the lanthanide zirconates is still needed in order to understand the mechanisms governing passivation film formation and elemental release rates more clearly.

In the last several years, there has been great interest amongst the ceramic community in high-entropy ceramics (HEC), which are typically defined as ceramic compounds with a composition of five or more principal cations in equimolar fractions. The Gibbs free energy ΔG offers a method to determine the thermodynamic stability of these complex ceramics through ΔG_{mix}, which can be expressed as:

$$\Delta G_{mix} = \Delta H_{mix} - T\Delta S_{mix} \quad (1)$$

where ΔH_{mix} is the mixing enthalpy of the compound, T is the temperature and ΔS_{mix} is the mixing configurational entropy which can further be expressed by equation 2

$$\Delta S_{mix} = -nR \sum_{i=1}^{N} x_i \ln x_i \quad (2)$$

where *n* is the molar ratio of the principal cations, *R* is the ideal gas constant, N is the number of element species in the principal cation sublattice and x_i is the molar fraction of the constituent *i* relative to the total constituents at the principal cation sublattice [15]. The gain in the formation enthalpy decreases with the number of species added and is eventually surpassed by the monotonic increase in entropy gain. Once this occurs, the compound is entropy stabilized [16]. This entropy stabilization is also accompanied by an increase in mass and size disorder of the mixed principal cations and has been shown to reduce thermal conductivity, increase elastic modulus and act as an impedance to the diffusion in several different materials [17, 18, 19, 20]. Wright et. al. (2020) compared the elastic modulus and thermal conductivity of 22 different high

and medium entropy pyrochlores to find correlations among the mixing configurational entropies, mass disorder (δ_{mass}), and size disorder (δ_{size}) of the cations on both sublattices [18]. They found the best correlation with the material properties occurred with size disorder, where increasing the size disorder of the pyrochlore led to an increase in elastic modulus and a decrease in thermal conductivity. The reduction in thermal conductivity was attributed to the large lattice distortions and oversized cages for smaller cations, which causes localized rattling of these cations and intensifies the scattering of heat-carrying phonons and decreases thermal conductivity [18, 21]. Yang et. al. (2020) also investigated the thermal-mechanical properties of several multicomponent titanate pyrochlores which showed comparable thermal conductivity and higher mechanical strength than single-component titanate pyrochlores [22].

In this study, equimolar multicomponent zirconate fluorites with a general chemical formula of $A_2Zr_2O_7$ (A= (Sm,Yb), (Sm,Yb,Gd), (Sm,Yb,Gd,Er), and (Sm,Yb,Gd,Er,Dy) in equimolar ratios) were synthesized using spark plasma sintering (SPS) to control their crystalline grain size. The as-sintered pellets were characterized by X-ray diffraction (XRD) to confirm their crystalline structures. Laboratory scale leaching tests are commonly used to estimate the chemical durability of waste form materials. However, different leaching protocols and conditions may result in significant differences in the elemental release rates of the same materials. Hence for a more direct comparison with the Yang et. al. (2021) study, the same semi-dynamic leaching experiments were performed in pH=1 nitric acid at 90 °C for 14 days. Scanning electron microscopy (SEM), Raman spectroscopy, Transmission electron microscopy (TEM), and Scanning-transmission electron microscopy (STEM) were used to characterize the surface of the zirconate samples post-leaching experiment. The release rates of the multicomponent zirconate fluorites were correlated with A-site size disorder and mixing entropy, and compared with the leaching behaviors of single-component zirconate fluorites to better understand the underlying mechanisms and the effects of key material parameters that govern their chemical durability. The percentage size disorder parameter for the multicomponent zirconate solid solutions used in this study is defined as [18]:

$$\delta_{\mathrm{mix}} = \sqrt{\sum_{i=0}^{n} x_i \left(1 - \frac{r_i}{r_{avg}}\right)^2} \qquad (3)$$

Where x_i is the atomic fraction and r_i is the radius of the i^{th} component in the A-site sublattice, r_{avg} is the overall weighted average of ionic radius, n stands for total molar concentration and R stands for ideal gas constant, 8.314 J mol^{-1} K^{-1}.

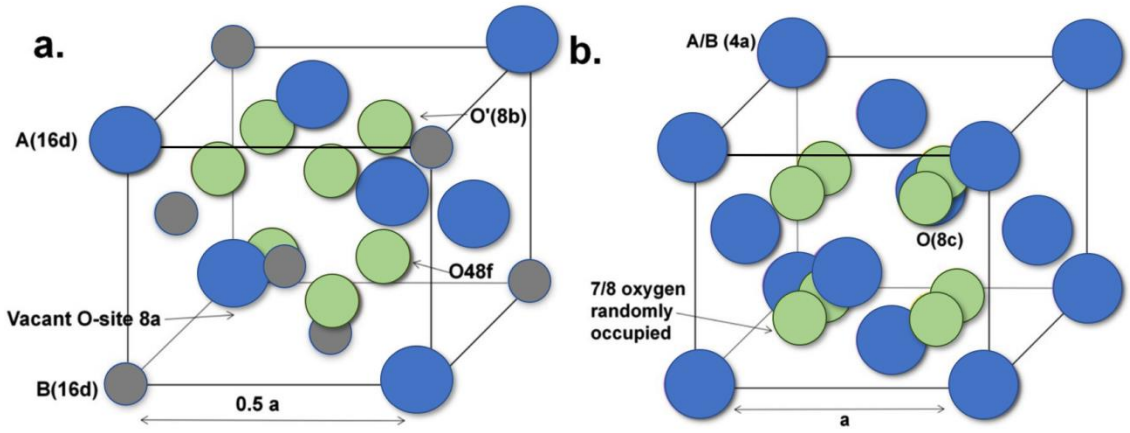

Fig. 1. Schematics of (a) ordered pyrochlore and (b) defect fluorite structure unit cells.

2. Experimental Method

2.1 Powder synthesis and pellet sintering

The multicomponent zirconate defect fluorite solid solutions were synthesized *via* solid-state reactions using ZrO_2, Sm_2O_3, Gd_2O_3, Dy_2O_3, Er_2O_3, and Yb_2O_3 as precursor materials. The mixture of precursor powders was milled by high-energy ball milling (HEBM) using ethanol as the mixing solvent and ZrO_2 milling balls as the grinding material. The powders were milled at 500 rpm for 80 cycles of 30-minute duration with 10-minute pauses in-between cycles. After milling, the slurry was dried at 85 °C for 12 hours and then calcined at 1000 °C for 12 hours. The milled powders were then ground into fine powders and loaded into 8 mm diameter cylindrical graphite dies and consolidated into dense pellets using SPS (Model 10−3 SPS system, Thermal Tech. LLC, Santa Rosa, CA). A steady flow of argon gas (1 L min−1) was used during the sintering process to purge the chamber to avoid oxidation of the graphite die. The powder samples were heated from room temperature to the sintering temperature of 1200 °C at a rate of 200 °C min^{-1}, then held at 1200 °C and under a uniaxial pressure of 40 MPa for 30 minutes. The

sintered pellets were then ground with SiC abrasive papers and then polished with 1 μm diamond paste to achieve a mirror finish with anhydrous ethanol acting as the polishing agent. Both top and bottom surfaces were polished as the whole pellets were subjected to leaching conditions.

2.2 Phase and microstructure characterization

The phase compositions of the sintered pellets were confirmed *via* X-ray diffraction (XRD) using a Panalytical X'Pert Pro system (Westborough, MA, USA) with a copper target (Kα = 0.15406 nm) and a step size of 0.013°. The physical density of the pellet was measured *via* the Archimedes technique using an Adam analytical scale (Danbury, NY, USA) with water used as the immersing medium. A measurement of the Raman shift at the pellet surface was performed before and after the leaching experiment, using a Raman spectrometer with a 514 nm laser, an exposure time of 10 s, and an operating power of 20 mW. The microstructures of the pellet samples were examined before and after the leaching experiments *via* SEM using an FEI Versa (USA). A STEM (FEI Titan, USA) system coupled with an EDS detector (Oxford Instruments, Abingdon, UK) was used to perform morphological, structural, and semi-quantitative elemental analysis of the sample surfaces post-leaching experiment. Lamellae were prepared for TEM/STEM characterization using the FEI Quanta 3D FEG dual-beam SEM FIB instrument. A platinum protection layer was deposited onto the cutting area of the leached pellet to reduce beam damage to the extracted lamellae. The extracted lamellae were thinned using a Ga ion source to ~100 nm *via* a series of decreasing ion beam currents.

2.3 Semi-dynamic leaching test

1-day and 14-day semi-dynamic leaching tests were conducted on the multicomponent zirconate pellets where high-purity pH=1 nitric acid was used as the leaching agent, following an ASTM C1308 leaching protocol [23]. The pellet was placed in the leaching agent in a sealed PTFE container with the pellet surface area to volume ratio (S/V) kept at 5.0 m^{-1} throughout the experiment. The semi-dynamic leaching experiments were conducted at 90 °C, where the leachates were exchanged at 3 hours intervals for the first 24 hours and then at 1-day intervals until the end of the 14-day leaching period. After the experiment, all the leachates collected were

filtered before elemental analysis *via* ICP-MS. The ICP-MS Varian 820 was used to measure the concentrations of leached elements in the collected leachates to calculate the corresponding leaching rates m_i (mg m^{-2} hr^{-1}/mg m^{-2} day^{-1}) using the following equation:

$$m_i = \frac{C_i V}{St} \tag{4}$$

where C_i is the concentration measured using ICP-MS (mg/L), V is the leachate volume (L), S is the surface area of the pellet (m^2) and *t* represents the sampling interval (3 hours or 1 day). The zirconates being investigated have different numbers of lanthanides at the A-site sublattice, and hence the leaching rates are normalized to accurately compare them between zirconates with different numbers of lanthanides at the A-site sublattice. The normalized release rates of each lanthanide element Nm_i (mg m^{-2} hr^{-1} or mg m^{-2} day^{-1}) are calculated by equation 5:

$$Nm_i = \frac{C_i V}{f_i St} \tag{5}$$

where f_i is the fraction of the lanthanide at the A-site position.

The initial release rates *k* (mg m^{-2} hr^{-1}) are obtained by a linear fitting of the A-site cumulative concentration *m(i)* (mg m^{-2}) of the bulk solution within the first 24 hours, assuming that the initial leaching was regulated solely by the dissolution mechanism. The long-term leaching rate (mg·m^{-2}·d^{-1}) was calculated based on a modified version of Cote's model [24] and is shown in equation 6, where the leaching rate is controlled by dissolution, surface effects, and diffusion:

$$m(t) = k_1 + \frac{1}{2} k_2 t^{-0.5} + k_3 k_4 e^{-k_4 t} \tag{6}$$

Here, m(t) stands for the leaching rate (mg·m^{-2} day^{-1}). The first term on the right side of equation 6, k_1, represents linear dissolution behavior; k_2 represents the mass transport by diffusion; and k_3 and k_4 stand for the species exchange between the matrix surface and solution. The long-term leaching rates can be calculated by first fitting the daily leaching rates to the diffusion-controlled mechanism in Cote's model (equation 7). The diffusion section of the 14-day release rate curves is fitted using equation 7 to determine the dissolution and diffusion parameters (k_1 and k_2) of the multicomponent zirconate solid solutions. Assuming an infinite duration for time (*t*), the release

rate will approach a constant value, and thus this rate constant for long-term release is determined to be the fitting parameter k_1.

$$m(t) = k_1 + \frac{1}{2}k_2 t^{-0.5} \quad (7)$$

3. Results and Discussion

3.1 Phase and microstructure evolution

The XRD patterns of the multicomponent zirconate defect fluorite sintered pellets are shown in Fig. 2(a), where all samples match the defect fluorite structure (*Fm*-$\bar{3}$*m*, space group #225) with no indication of secondary phases, except for a minor pyrochlore peak observed from the XRD pattern of $(Sm,Gd,Yb)_2Zr_2O_7$. This is expected as $(Sm,Gd,Yb)_2Zr_2O_7$ has the largest r_A/r_B radius ratio of 1.44, which borders on the 1.48-1.72 range needed for the ordered pyrochlore to be stabilized. The lattice parameters of each multicomponent zirconate defect fluorite were calculated through peak refinement using the MDI Jade 6.5 software and plotted against the average ionic radius of the A-site cations as shown in Fig. 2(b). The plot shows an increase in lattice parameter with increased average ionic radius, which is the trend generally observed in single-component zirconate defect fluorites, as having large-sized cations at the A-site, *i.e.*, Sm and Gd, causes more lattice expansion [14]. The same trend is observed at the highlighted (400) reflection, which shows a shift to a lower angle with an increased average ionic radius.

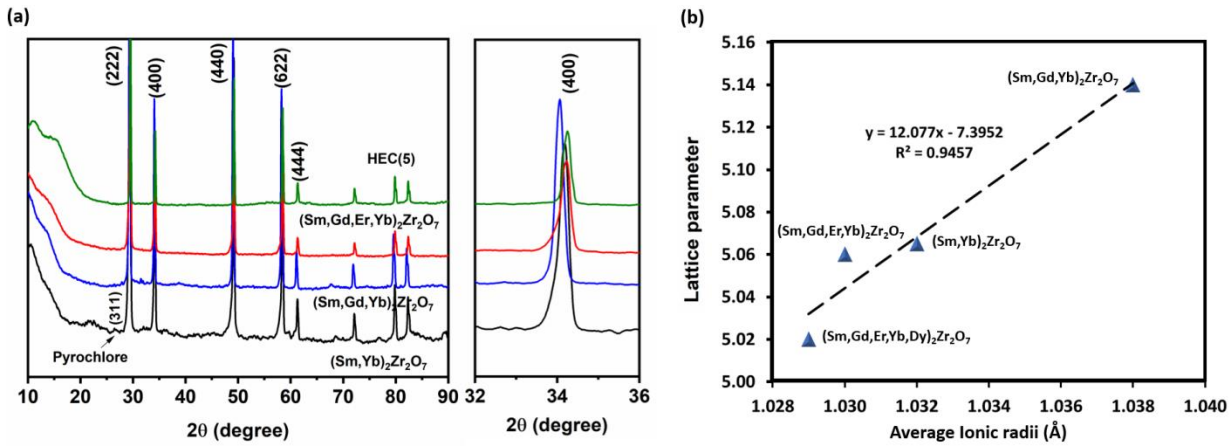

Fig. 2. (a) XRD patterns of as-sintered multicomponent zirconate defect fluorites; (b) the correlation between the average ionic radius and the unit cell lattice parameter.

Figs. 3(e)-(h) show the surface microstructure of the four multicomponent zirconates post 14-days leaching, where a dense passivation layer has homogeneously covered the leached surface, and the grain structures of the pristine pellets shown in Figs. 3(a)-(d) are no longer visible. Similar passivation layers have been reported for single-component lanthanide zirconates, with the passivation layer being enriched in either lanthanides or zirconium, depending on the composition of the zirconate [14]. The Raman spectra of the pristine and 14-day leached multicomponent zirconates are shown in Figs. 4(a)-(d). The T_{2g} Raman peak is clearly visible in all four samples and is characteristic of the Zr-O spectral band [25]. There is considerable broadening of the Raman peaks likely due to the departure from translational periodicity found in the pyrochlore system to the more structurally disordered defect fluorite system, with random vacancy positions present in the oxygen sublattice [5].

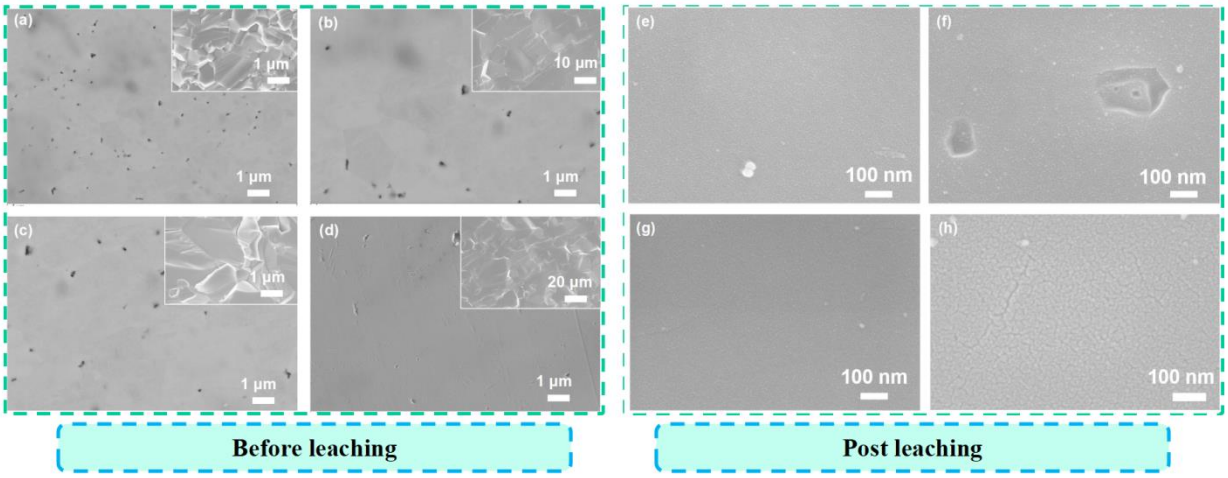

Fig. 3. (a-d) SEM images of the polished surface and fracture cross-section of pristine $(Sm,Yb)_2Zr_2O_7$, $(Sm,Yb,Gd)_2Zr_2O_7$, $(Sm,Yb,Gd,Er)_2Zr_2O_7$, and $(Sm,Yb,Gd,Er,Dy)_2Zr_2O_7$ pellets respectively; (e-h) SEM images of $(Sm,Yb)_2Zr_2O_7$, $(Sm,Yb,Gd)_2Zr_2O_7$, $(Sm,Yb,Gd,Er)_2Zr_2O_7$, and $(Sm,Yb,Gd,Er,Dy)_2Zr_2O_7$ pellets respectively post 14 days leaching tests at 90 °C in nitric acid solution pH = 1.0.

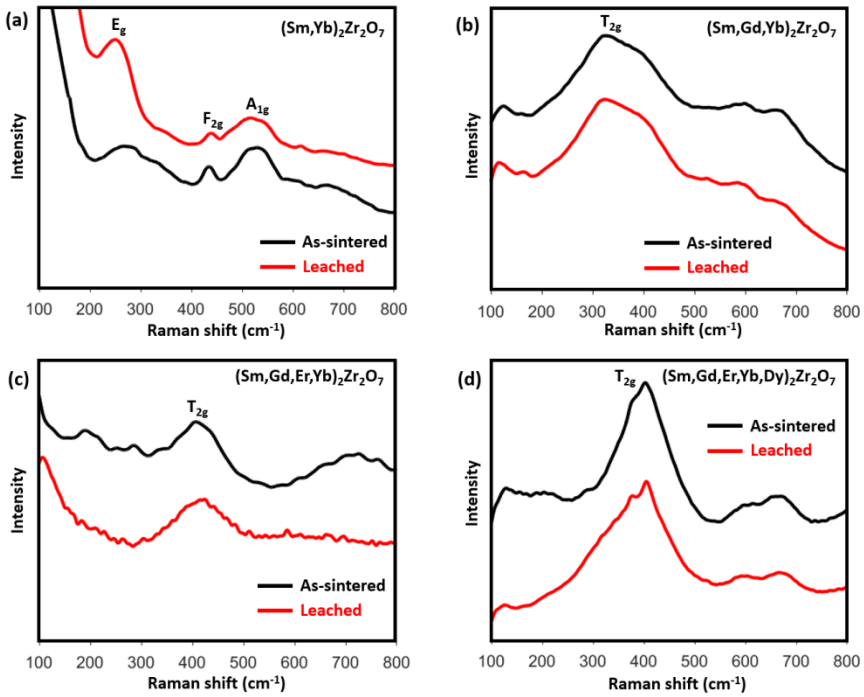

Fig. 4. Raman Spectra of $(Sm,Yb)_2Zr_2O_7$, $(Sm,Yb,Gd)_2Zr_2O_7$, $(Sm,Yb,Gd,Er)_2Zr_2O_7$, and $(Sm,Yb,Gd,Er,Dy)_2Zr_2O_7$ before and post 14-day leaching tests at 90 °C in nitric acid solution pH = 1.0.

TEM-STEM analysis was performed on the cross-section of the leached $(Sm,Yb,Gd,Er,Dy)_2Zr_2O_7$ sample to investigate the structure and composition of the surface alteration layers. Fig. 5(a) shows the cross-sectional TEM image along the [101] zone axis of the $(Sm,Yb,Gd,Er,Dy)_2Zr_2O_7$ lamella, indicating three different layer structures. An altered surface layer approximately 5-8 nm thick is shown in Figs. 5(b)-(c), located beneath the Pt layer at the top surface. The corresponding inversely fast Fourier transferred (IFFT) image identifies the surface alteration layer film as having a defect fluorite structure with some amount of amorphization indicated by the amorphous halo. Fig. 5(d) shows the matrix beneath the alteration layer, which appears to have a less uniform structure and scattering diffraction compared to the unreacted matrix shown in Fig. 5(e), where the unreacted matrix shows a perfect lattice arrangement without diffraction scattering. The diffusion scattering in the alteration matrix suggests damage domains of the defect fluorite structure though no amorphous halos. The transition from the highly uniform unreacted matrix to the more disordered structure is gradual over a 200-250 nm range. Overall, this result suggests a corrosion-induced amorphization from the original defect fluorite structure to a less crystalline defect fluorite structure at the alteration layer. The d-spacing of the (111) plane of the $(Sm,Yb,Gd,Er,Dy)_2Zr_2O_7$ unreacted matrix is 0.290 nm, which corresponds to a lattice parameter of 5.029 Å. This value closely agrees with the lattice parameter calculated from the XRD pattern peak refinement. The d-spacings measured at the altered matrix regions are also similar to that of the unreacted matrix, indicating that there is no significant lattice distortion between these locations. Fig. 5(g) shows the EDS line scan profiles measured along the line indicated in the BF STEM image in Fig. 5(f). An initial enrichment in the total quantity of lanthanide elements is observed over the first 5 nm, corresponding to the 5~8 nm surface alteration layer depleted with Zr. No significant depletion of the lanthanides or zirconium occurred after the initial few nanometers, and the atomic ratios remain relatively close to the stoichiometric ratios. These results indicate that there are no

significant chemical differences between the alteration layer, the altered matrix, and the unreacted matrix except the top few nm-thick surface layer.

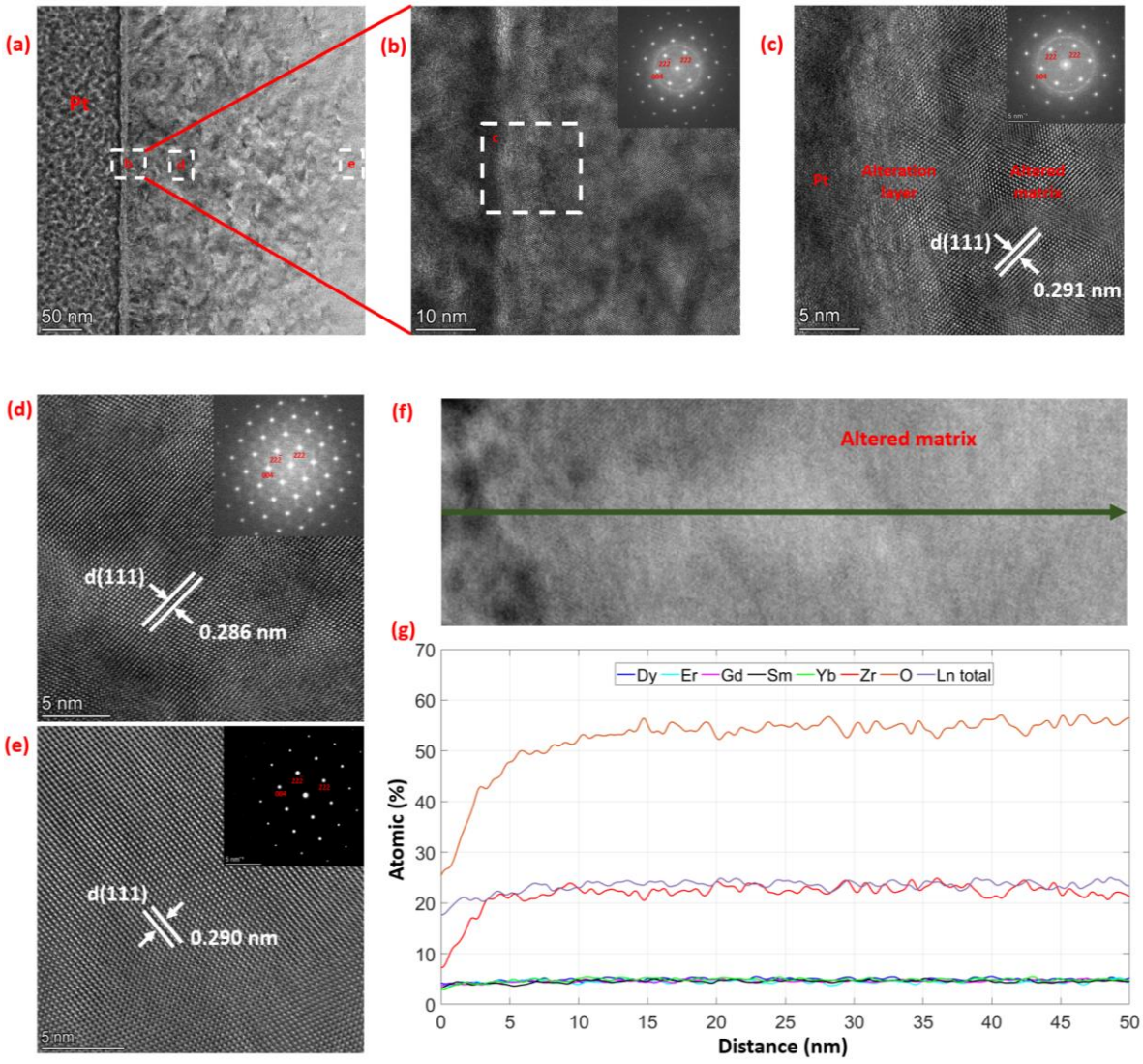

Fig. 5. TEM images showing the surface alteration and microstructure of the $(Sm,Yb,Gd,Er,Dy)_2Zr_2O_7$ after 14 days of leaching at 90 °C in a solution of nitric acid at pH 1.0. (a) A thin cross-section TEM lamella of the leaching surface prepared by FIB; (b) a TEM image of the surface alteration layer and an IFFT image of the entire area; (c) a high-resolution TEM image of the platinum layer at the pellet surface, the alteration layer and the altered matrix; (d) a high-resolution TEM image of the altered matrix and an IFFT image of the area; (e) a high-resolution TEM image of the unreacted matrix and the SAED pattern taken from the area

showing the defect fluorite structure; (f-g) BF STEM image and the corresponding EDS line scan profiles 65 nm along the depth of the lamella.

3.2 Elemental release rates and corrosion mechanisms

ICP-MS was used to analyze the elemental concentrations of the leachate after semi-dynamic leaching testing in aqueous solutions at 90 °C in pH=1 nitric acid. The concentration of each element in the leachate can be used to estimate the element release rate in order to investigate their correlations with material and structural parameters, and to better quantify their chemical durability. The normalized release rates of the A-site cations are shown in Figs. 6(a)-(d), where there is an initial rapid release of the elements followed by a gradual reduction of the release rates. This could be a result of the formation of the surface alteration layer, which reduces the interaction between water molecules and the bulk material, and thus the elemental release rates. This behavior is typical for the dissolution of ceramics.

Fig. 6(a) shows the normalized release rates of A-site cations of $(Sm,Yb)_2Zr_2O_7$ for up to 14 days. Sm displays a higher release rate than Yb, which is expected as the A-site release rates of single-component zirconates have been shown to decrease with the reduction of the ionic size of lanthanides [14]. This trend continues and is shown in Figs. 6(b)-(c) as the Gd release rates are close to those of Sm, and the Er release rates are slightly higher than those of Yb. However, the trend does not explain the greatly reduced release rates of Gd and Sm observed in the high entropy ceramic as compared with other multicomponent components. The larger-sized lanthanides, e.g., Gd and Sm, show comparable release rates as smaller-sized lanthanides (Dy, Er, and Yb) Fig. 6(d). A possible explanation could be that by adding new species, the mixing entropy increases, which would decrease element segregation and lead to a smaller difference in the release rates of the individual elements [26]. These results also imply significant structural distortion and change in the bond environment of the polyhedron when increasing the number of components to high entropy zirconate.

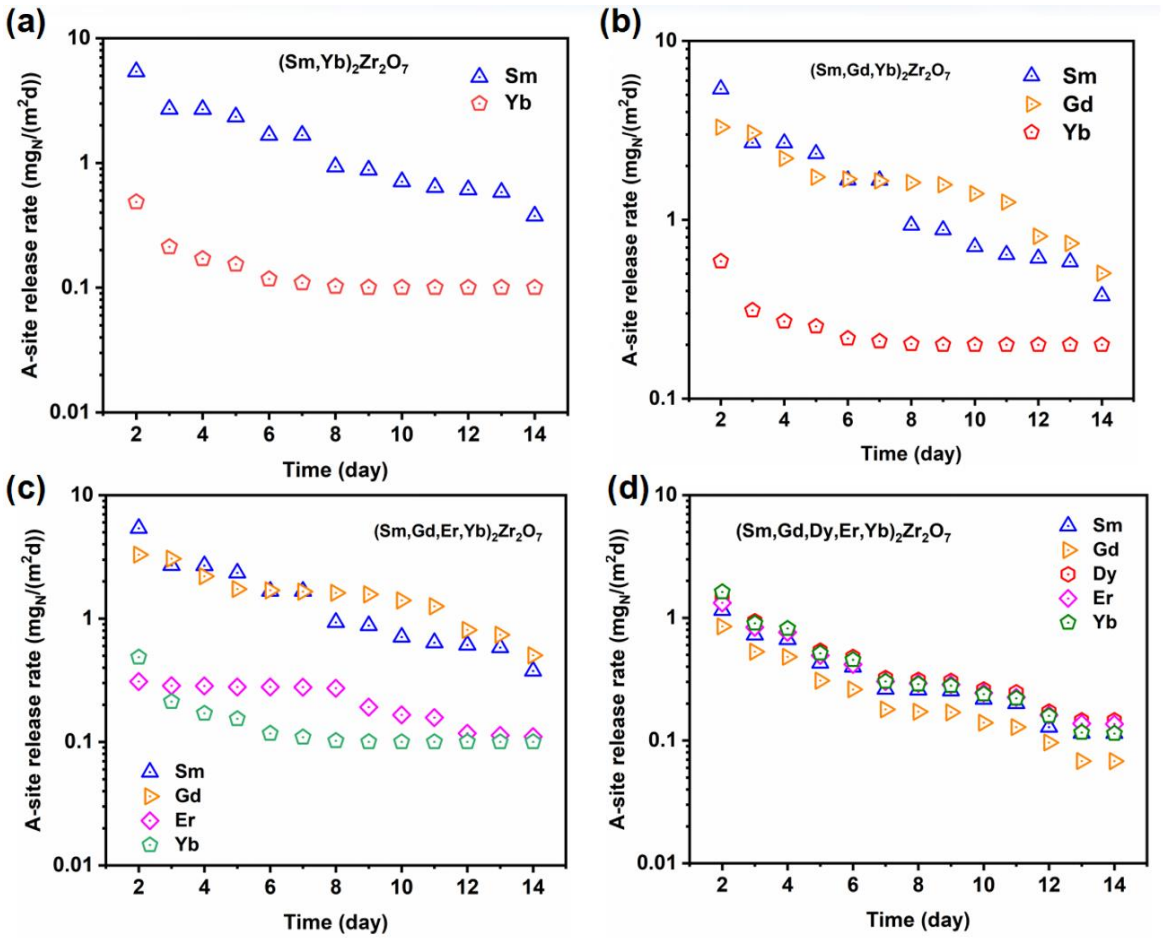

Fig. 6. (a-d) long-term (14-days) A-site cation normalized release rates for $(Sm,Yb)_2Zr_2O_7$, $(Sm,Yb,Gd)_2Zr_2O_7$, $(Sm,Yb,Gd,Er)_2Zr_2O_7$, and $(Sm,Yb,Gd,Er,Dy)_2Zr_2O_7$ at 90 °C in a solution of nitric acid at pH = 1.0.

Figs. 7(a)-(b) show the sum of the short-term and long-term release rates of the A-site cations in multicomponent zirconates. These release rates are relatively close compared to the large variation in release rates observed in their constituent single-component zirconates [14]. Fig 7(a) shows a sharp decrease in A-site release rate followed by relatively constant release rates, this occurs after 9 hours for $(Sm,Yb)_2Zr_2O_7$ and $(Sm,Yb,Gd,Er,Dy)_2Zr_2O_7$, and after 15 and 21 hours for $(Sm,Yb,Gd)_2Zr_2O_7$ and $(Sm,Yb,Gd,Er)_2Zr_2O_7$ respectively. The initial decrease in dissolution rates may be attributed to the change in dissolution sites from high-energy surface sites, such as grain boundaries, to dissolution on the edges, kinks, and etch pits of grain surfaces [27]. Fig. 7(b) displays the long-term release rates of the A-site cations in the multicomponent

zirconates. Among the samples, $(Sm,Yb,Gd,Er,Dy)_2Zr_2O_7$ exhibits the lowest release rates, clearly transitioning to a diffusion-controlled leaching mechanism after 8 days. The comparison between the short and long-term release rates is depicted in Fig. 7(c). The initial matrix dissolution regime persists for the first 2 days of leaching, with relatively constant leaching rates following the initial rapid release. The transition state extends from day 2, but the specific point of transition to a diffusion-controlled mechanism varies among the samples. $(Sm,Yb,Gd,Er)_2Zr_2O_7$ and $(Sm,Yb,Gd,Er,Dy)_2Zr_2O_7$ undergo a transition to a diffusion-controlled release mechanism on day 8, while the transition for $(Sm,Yb)_2Zr_2O_7$ and $(Sm,Yb,Gd)_2Zr_2O_7$ appears to be more gradual. The leaching rates for all samples approach a constant value within the diffusion-controlled regime. Assuming a dissolution-controlled leaching mechanism within the first 24 hours, the cumulative mass release was linearly fitted using equation 7 to calculate the short-term rate constant, while the 14-day leaching rates were fitted using equation 6. All fitting parameters are listed in Table S1, with the short-term and long-term reaction rates, listed in Table 1. Overall, high entropy $(Sm,Yb,Gd,Er,Dy)_2Zr_2O_7$ demonstrates the lowest short-term and long-term release rates, measuring 4.040 mg m^{-2} d^{-1} and 0.223 mg m^{-2} d^{-1}, respectively. These findings imply a slow growth of the surface passivation film for high entropy materials as compared to the solid solution with lower numbers of elements.

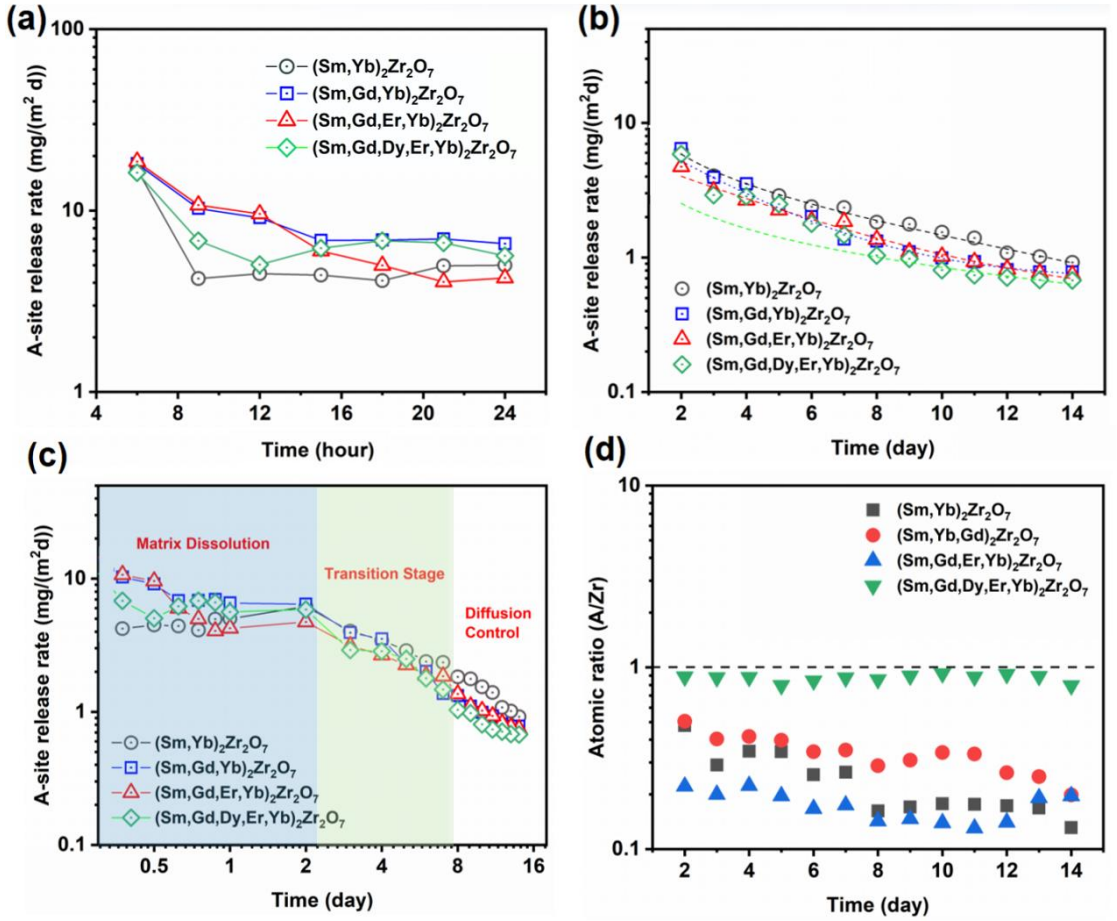

Fig. 7. (a-b) short term (1-day) and long-term (14-days) total A-site cation release rates for $(Sm,Yb)_2Zr_2O_7$, $(Sm,Yb,Gd)_2Zr_2O_7$, $(Sm,Yb,Gd,Er)_2Zr_2O_7$, and (Sm,Yb,Gd,Er,Dy)2Zr2O7 at 90 °C in a solution of nitric acid at pH = 1.0; (c) short-term (1-day) and long-term (14-days) A-site cation release rates; (d) Corresponding atomic ratios (A/Zr) for 14-days leaching testing.

Table 1. Initial and long-term A-site release rates

	Sm,Yb	Sm,Yb,Gd	Sm,Yb,Gd,Er	Sm,Yb,Gd,Er,Dy
initial	**6.96**	**6.63**	**4.96**	**4.04**
14-days	**0.68**	**0.44**	**0.32**	**0.22**

Table 1 displays the initial and long-term A-site release rates, which were determined by fitting the A-site cumulative concentration and leaching rates. The fitting parameters from Cote's equation are provided in Table S1. For a clearer understanding of the underlying mechanism of the multicomponent zirconate dissolution behavior, the initial and long-term A-site release rates listed in Table 1 were plotted against material parameters such as ionic radius ratio, lattice parameter, A-site cation size disorder, and mixing entropy. XRD refinement was used to derive the lattice parameters, while mixing entropy and A-site cation size disorder were calculated from equations 2 and 3, respectively. Fig. 8 shows the plot of the release rates versus the previously mentioned material parameters. There is a small positive correlation with both the ionic radius ratio and lattice parameter shown in Figs. 10(a)-(b), a strong positive correlation with A-site cation size disorder indicated in Fig. 10(c), and a negative correlation with entropy mixing shown in Fig. 10(d). The elemental release rates of single-component lanthanide zirconates have been shown to decrease with the reduction of the A-site ionic radius, leading to shorter and stronger metal-oxygen bonds (A-O bonds) in the coordinated polyhedron [28, 14, 29]. Therefore, a positive correlation of A-site ionic radius with elemental release rates is expected within this range. However, the correlation is low due to $(Sm,Yb)_2Zr_2O_7$ having higher release rates than $(Sm,Yb,Gd)_2Zr_2O_7$, which has a larger ionic radius ratio. This indicates that there are additional factors contributing to the stability of the multicomponent zirconates beyond the metal-oxygen bonds of the A-site cations. Fig. 10(b) shows a similar correlation between the lattice parameters and the elemental release rates, which is expected, as the lattice parameter is directly related to the ionic radius of the cations at the A-site position. An increase in cation size disorder generally corresponds with an increase in lattice distortion, which has been shown to cause sluggish outward diffusion of cations from their host matrix and sluggish inward diffusion of corrosive species such as water molecules. This sluggish diffusion was demonstrated by Tan et. al (2020) through the oxidation of high entropy transitional metal carbides in 1200 °C water vapor [20]. However, the positive correlation with A-site cation size disorder shown in Fig. 10(c) stands in contrast to this expectation and the results of the study by Yang et. al (2023) [30]. Specifically, the elemental release rates of multicomponent lanthanide titanate pyrochlores were negatively correlated with the A-site cation size disorder, indicating that the disordering at the defect fluorite cation sublattice is also having an additional effect on the chemical durability of the zirconates. On the other hand, Fig. 10(d) shows a clear decrease in the release rates of the

multicomponent zirconates with increased mixing entropy (ΔS_{mix}). This increase in corrosion resistance may be attributed to the likely decreases in elemental segregation and increased phase stability of the entropy stabilized compounds [26].

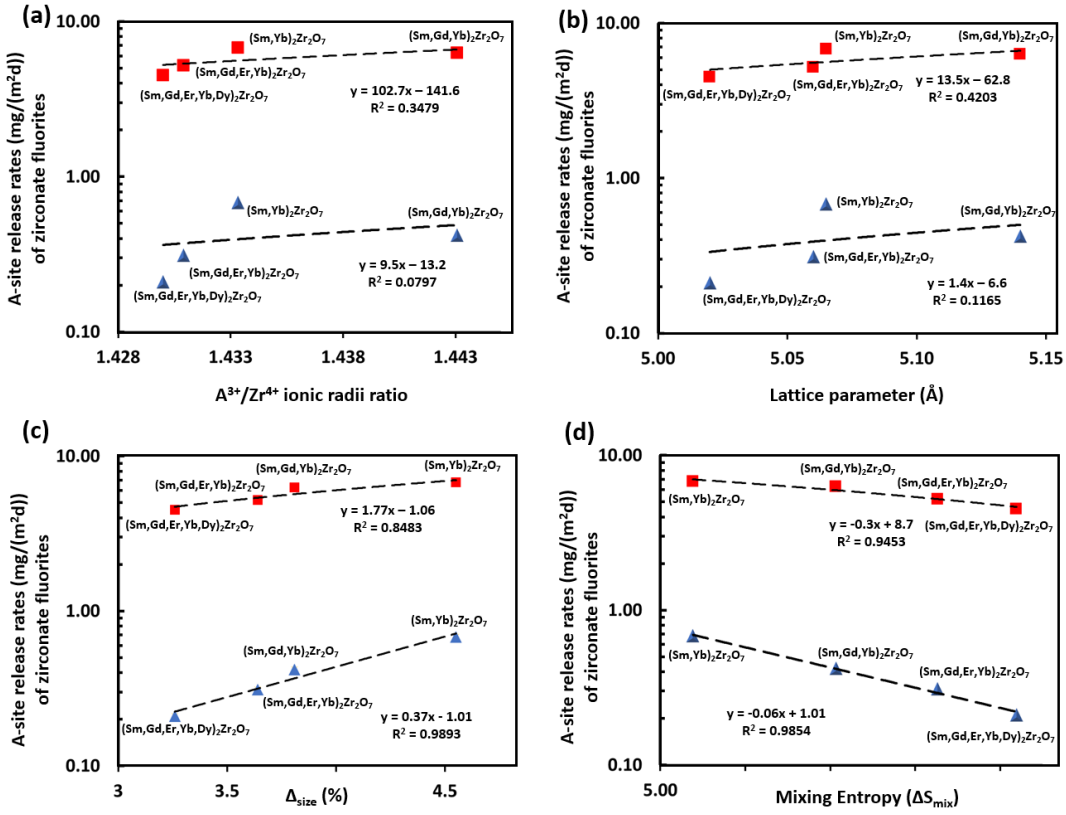

Fig. 8. Initial (red symbol) and long-term (blue symbol) elemental release rates of zirconate fluorite versus (a) ionic radii ratio, (b) lattice parameter, (c) A-site cation size disorder, and (d) mixing entropy.

It is also observed that the initial and long-term release rates of the multicomponent zirconates are relatively close to each other ranging from 4.5 to 6.8 mg m^{-2} day^{-1} and 0.21 to 0.68 mg m^{-2} day^{-1}, compared to their single-component constituents ($Yb_2Zr_2O_7$ – $Sm_2Zr_2O_7$) which varied from 1.0 to 516.5 mg m^{-2} day^{-1} in the initial term and 1.0 x10^{-6} to 0.13 mg m^{-2} day^{-1} in the long-term [30]. The initial release rates of the multicomponent zirconates are comparatively closer to those of $Er_2Zr_2O_7$ and $Yb_2Zr_2O_7$ and are significantly reduced compared to $Dy_2Zr_2O_7$, $Gd_2Zr_2O_7$, and $Sm_2Zr_2O_7$. However, all the long-term release rates of the multicomponent zirconates were higher than those of their single-component constituents. This could be due to

the mixing entropy effect, leading to improved chemical durability during the dissolution-controlled section of the leaching experiment, but being less effective once the leaching behavior changes to a diffusion-controlled mechanism. This leads to the conclusion that the sluggish diffusion effect caused by lattice distortion is not the dominant high entropy effect contributing to the chemical durability of the multicomponent zirconates. Overall, A-site cation size disorder and mixing entropy show a strong correlation with A-site elemental release rates, but larger sets of multicomponent zirconates need to be tested to better understand these trends. Further investigation is also needed to understand the effects of A-site cation mixing on empirical material parameters, such as the A-O metal-oxygen bond strengths and the oxygen positional parameter x_{48f}. This will aid in better predicting the dissolution rates and chemical durability of multicomponent pyrochlore and zirconate fluorites.

4. Conclusion

In conclusion, multicomponent lanthanide zirconates ($A_2Zr_2O_7$, A= (Sm,Yb), (Sm,Yb,Gd), (Sm,Yb,Gd,Er), and (Sm,Yb,Gd,Er,Dy)) were synthesized by SPS as potential nuclear waste forms. The chemical durability of the zirconate fluorites was evaluated *via* semi-dynamic leaching tests in pH=1 nitric acid at 90 °C. This was to facilitate more systematic comparisons between the leaching mechanisms for the multicomponent zirconates and previously studied single-component fluorites. $(Sm,Yb,Gd,Er,Dy)_2Zr_2O_7$ showed the lowest initial and long-term release rates of the multicomponent zirconates and was the only sample to demonstrate congruent dissolution, whereas the other multicomponent zirconates showed incongruent dissolution with the preferential release of zirconium. TEM analysis revealed the transition of $(Sm,Yb,Gd,Er,Dy)_2Zr_2O_7$ from defect fluorite to a more amorphized structure during the formation of the surface alteration layer; however, no significant chemical change was observed at the $(Sm,Yb,Gd,Er,Dy)_2Zr_2O_7$ altered matrix. Unlike the single-component fluorites, the ionic radius ratio of the multicomponent fluorites does not exhibit a clear correlation with elemental release rates. However, the elemental release rates show a positive correlation with the A-site cation disorder but a strong negative correlation with mixing entropy. Further understanding of corrosion kinetics and mechanisms governing the formation of passivation

films of multicomponent fluorites will be useful to predict long-term elemental release rates and design more chemically durable fluorites.

Acknowledgment

The synthesis of the multicomponent zirconate fluorites was supported by NSF under the Award DMREF-2119423. The dissolution testing of the multicomponent pyrochlore solid solution was supported as part of the Center for Performance and Design of Nuclear Waste Forms and Containers (WastePD), an Energy Frontier Research Center (EFRC) funded by the U.S. Department of Energy, Office of Science, Basic Energy Sciences under Award DE-SC0016584.

Declaration of Competing Interest

The authors declare that they have no conflict of interest.

References

[1] A. Ringwood, S. Kesson, N. Ware, W. Hibberson and A. Major, "The SYNROC process: A geochemical approach to nuclear waste immobilization," *Geochemical Journal,* vol. 13, no. 4, pp. 141-165, 1979.

[2] X. Guo, S. Gin, P. Lei, T. Yao, . H. Liu, D. K. Schreiber, D. Ngo, G. Viswanathan, T. Li, S. H. Kim, J. D. Vienna, J. V. Ryan, J. Du, J. Lian and G. S. Frankel, "Self-accelerated corrosion of nuclear waste forms at material interfaces," *Nature materials,* vol. 19, no. 3, pp. 310-316, 2020.

[3] F. v. Hippel, R. Ewing, R. Garwin and A. Macfarlane, "Time to bury plutonium," *Nature,* vol. 485, no. 7397, pp. 167-168, 2012.

[4] J. Lian, K. B. Helean, B. J. Kennedy, L. M. Wang, A. Navrotsky and R. C. Ewing, "Effect of structure and thermodynamic stability on the response of lanthanide stannate

pyrochlores to ion beam irradiation," *The Journal of Physical Chemistry B,* vol. 110, no. 5, p. 2343–2350, 2006.

[5] B. P. Mandal, M. Pandey and A. K. Tyagi, "Gd2Zr2O7 pyrochlore: potential host matrix for some constituents of thoria based reactor's waste," *Journal of Nuclear Materials,* vol. 406, no. 2, pp. 238-243, 2010.

[6] M. Glerup, O. F. Nielsen and F. W. Poulsen, "The structural transformation from the pyrochlore structure, A2B2O7, to the fluorite structure, AO2, studied by Raman spectroscopy and defect chemistry modeling," *Journal of Solid State Chemistry,* vol. 160, no. 1, pp. 25-32, 2001.

[7] L. Minervini, R. W. Grimes and K. E. Sickafus, "Disorder in pyrochlore oxides," *Journal of the American Ceramic Society,* vol. 83, no. 8, pp. 1873-1878, 2000.

[8] M. Jafar, P. Sengupta, S. N. Achary and A. K. Tyagi, "Phase evolution and microstructural studies in CaZrTi2O7 (zirconolite)–Sm2Ti2O7 (pyrochlore) system," *Journal of the European Ceramic Society,* vol. 34, no. 16, pp. 4373-4381, 2014.

[9] J. Wang, J. Wang, Y. Zhang, Y. Li, Y. Teng, Z. Wang and H. Tan, "Flux synthesis and chemical stability of Nd and Ce co-doped (Gd1− xNdx) 2 (Zr1− xCex) 2O7 (0≤ x≤ 1) pyrochlore ceramics for nuclear waste forms," *Ceramics international,* vol. 43, no. 18, pp. 17064-17070, 2017.

[10] S. J. Patwe, V. Katari, N. P. Salke, S. K. Deshpande, R. Rao, M. K. Gupta, R. Mittal, S. N. Achary and A. K. Tyagi, "Structural and electrical properties of layered perovskite type Pr2Ti2O7: experimental and theoretical investigations," *Journal of Materials Chemistry C,* vol. 3, no. 17, pp. 4570-4584, 2015.

[11] L. Wang, X. Shu, F. Yi, D. Shao, K. Zhang, H. Zhang and X. Lu, "Rapid fabrication and phase transition of Nd and Ce co-doped Gd2Zr2O7 ceramics by SPS," *Journal of the European Ceramic Society,* vol. 38, no. 7, pp. 2863-2870, 2018.

[12] S. Lutique, D. Staicu, R. J. M. Konings, V. V. Rondinella, J. Somers and T. Wiss, "Zirconate pyrochlore as a transmutation target: thermal behaviour and radiation resistance against fission fragment impact," *Journal of Nuclear Materials,* vol. 319, pp. 59-64, 2003.

[13] N. S. Kumar, N. C. Shekar and P. C. Sahu, "Pressure induced structural transformation of pyrochlore Gd2Zr2O7," *Solid State Communications ,* vol. 147, no. 9-10, pp. 357-359, 2008.

[14] K. Yang, Y. Wang, P. Lei, T. Yao, D. Zhao and J. Lian, "Chemical durability and surface alteration of lanthanide zirconates (A2Zr2O7: A= La-Yb)," *Journal of the European Ceramic Society,* vol. 41, no. 12, pp. 6018-6028, 2021.

[15] B. Ye, T. Wen, M. C. Nguyen, L. Hao, C.-Z. Wang and Y. Chu, "First-principles study, fabrication, and characterization of (Zr0.25Nb0.25Ti0.25V0.25)C high-entropy ceramics," *Acta Materialia,* vol. 170, pp. 15-23, 2019.

[16] P. Sarker, T. Harrington, C. Toher, C. Oses, M. Samiee, J.-P. Maria, D. W. Brenner, K. S. Vecchio and S. Curtarolo, "High-entropy high-hardness metal carbides discovered by entropy descriptors," *Nature communications,* vol. 9, no. 1, pp. 1-10, 2018.

[17] C. Ng, S. Guo, J. Luan, S. Shi and C. T. Liu, "Entropy-driven phase stability and slow diffusion kinetics in an Al0.5CoCrCuFeNi high entropy alloy," *Intermetallics,* vol. 31, pp. 165-172, 2012.

[18] A. J. Wright, Q. Wang, S.-T. Ko, K. M. Chung, R. Chen and J. Luo, "Size disorder as a descriptor for predicting reduced thermal conductivity in medium- and high-entropy pyrochlore oxides," *Scripta Materialia,* vol. 181, pp. 76-81, 2020.

[19] C. M. Rost, E. Sachet, T. Borman, A. Moballegh, E. C. Dickey, D. Hou, J. L. Jones, S. Curtarolo and J.-P. Maria, "Entropy-stabilized oxides," *Nature communications,* vol. 6, no. 1, pp. 1-8, 2015.

[20] Y. Tan, C. Chen, S. Li, X. Han, J. Xue, T. Liu, X. Zhou and H. Zhang, "Oxidation behaviors of high-entropy transition metal carbides in 1200 °C water vapor," *Journal of Alloys and Compounds,* vol. 816, p. 152523, 2020.

[21] A. J. Wright and J. Luo, "A step forward from high-entropy ceramics to compositionally complex ceramics: a new perspective," *Journal of Materials Science,* vol. 55, no. 23, pp. 9812-9827, 2020.

[22] K. Yang, K. Bryce, W. Zhu, D. Zhao and J. Lian, "Multicomponent pyrochlore solid solutions with uranium incorporation – A new perspective of materials design for nuclear applications," *Journal of the European Ceramic Society,* vol. 41, no. 4, pp. 2870-2882, 2021.

[23] *ASTM-C1308-08. Accelerated Leach Test for Diffusive Releases From Solidified Waste and a Computer Program to Model Diffusive, Fractional Leaching From Cylindrical Waste Forms.,* West Conshohocken, PA: ASTM International, 2009.

[24] P. L. Cote, T. W. Constable and A. Moreira, "An evaluation of cement-based waste forms using the results of approximately two years of dynamic leaching," *Nuclear and chemical waste management,* vol. 7, no. 2, pp. 129-139, 1987.

[25] U. A. Renju and P. P. Rao, "Defect fluorite type phase in anion deficient rare earth zirconates, RE3Zr0. 5Nb0. 5O6. 75 (RE= Nd, Sm, Gd, Dy, Y): Synthesis and electrical properties," *Journal of Solid State Chemistry,* vol. 293, p. 121754, 2021.

[26] Y. Fu, J. Li, H. Luo, C. Du and X. Li, "Recent advances on environmental corrosion behavior and mechanism of high-entropy alloys," *Journal of Materials Science & Technology,* vol. 80, pp. 217-233, 2021.

[27] A. Lüttge, R. S. Arvidson and C. Fischer, "A stochastic treatment of crystal dissolution kinetics," *Elements,* vol. 9, no. 3, pp. 183-188, 2013.

[28] K. Yang, P. Lei, T. Yao, B. Gong, Y. Wang, M. Li, J. Wang and J. Lian, "A systematic study of lanthanide titanates (A2Ti2O7) chemical durability: corrosion mechanisms and control parameters," *Corrosion Science,* vol. 185, p. 109394, 2021.

[29] B. Gong, K. Yang, J. A. Lian and J. Wang, "Machine learning-enabled prediction of chemical durability of A2B2O7 pyrochlore and fluorite," *Computational Materials Science,* vol. 200, p. 110820, 2021.

[30] K. Yang, K. Bryce and J. Lian, "Chemical durability and microstructure evolution of compositional complex titanate pyrochlore waste forms with uranium incorporation," 2023.